npj computational materials

www.nature.com/npjcompumats

ARTICLE OPEN

Check for updates

Topology-enhanced mechanical stability of swelling nanoporous electrodes

Benjamin E. Grossman-Ponemon[1,2], Ataollah Mesgarnejad[1] and Alain Karma[1]✉

Materials like silicon and germanium offer a 10-fold improvement in charge capacity over conventional graphite anodes in lithium-ion batteries but experience a roughly threefold volume increase during lithiation, which challenges ensuring battery integrity. Nanoporous silicon, created by liquid-metal-dealloying, is a potentially attractive anode design to mitigate this challenge, exhibiting both higher capacity and extended cycle lifetimes. However, how nanoporous structures accommodate the large volume change is unknown. Here, we address this question by using phase-field modeling to produce nanoporous particles and to investigate their elastoplastic swelling behavior and fracture. Our simulations show that enhanced mechanical stability results from the network topology consisting of ligaments connected by bulbous, sphere-like nodes. The ligaments forcefully resist elongation while the nodes, behaving like isolated spherical particles, experience large stresses driving fracture. However, being smaller compared to a sphere of the same volume as the entire nanoporous particle, the nodes are more protected against fracture.

npj Computational Materials (2023)9:116 ; https://doi.org/10.1038/s41524-023-01047-y

INTRODUCTION

With approximately ten times greater gravimetric charge capacity over conventional carbon-based anodes, silicon and germanium have emerged as attractive anode materials for lithium-ion batteries[1]. Instead of lithium ion intercalation, such anodes operate via alloying, transforming crystalline or amorphous Si/Ge (c- or a-Si/Ge) into an amorphous phase (a-Li_xSi or a-Li_xGe)[2]. Along with improved charge capacity, the alloying process produces a nearly 300% volume change in the anode[3], which can lead to mechanical failure, thereby preventing these materials from seeing their full potential.

Fracture is a major failure mode in silicon and germanium anodes[4]. The large volume change during lithiation can result in tensile stress buildup at the anode surface, causing both pulverization[3,5] (due to networks of small surface cracks) and even complete rupture[4]. Such fractures result in loss of electrical contact in the anode. The volume change and fractures also impact the stability of the solid-electrolyte interphase (SEI), a passivation layer which builds upon the anode surface during cell operation. Repeated damage to the SEI can result in continued accumulation of passivated material, which causes large capacity fade[5,6].

There are several factors in anode design that affect fracture. Anode size is most notable, with experiments showing that larger particles are more prone to cracking[4,7–9]. The size effect results from two sources. First, the stress fields which develop during lithiation are approximately scale invariant (the only length scale that appears is the interface thickness between lithiated and unlithiated phases, which is generally small compared with particle sizes explored in the literature[2]), whereas from dimensional analysis fracture is length-dependent, characterized by the toughness G_c. Hence, a long crack in a large particle is more likely to break than a short crack in a small particle, even if the crack length-to-particle diameter ratios are identical. Second, as shown analytically[9], highly symmetrical shapes like spheres and wires have large tensile stresses on the surface, but compressive stresses within. The gradient in the stress is more pronounced in smaller particles, when the flaw size is comparable to the particle radius. As demonstrated computationally in ref. [4], the stress gradient leads to reduced stresses over the length of the flaw, thereby lowering the crack driving force.

Particular to crystalline silicon[10] and germanium[11] is the effect of anisotropic speed of invasion of the c-Si/a-Li_xSi interface. In highly-symmetric shapes like wires or pillars, as c-Si or c-Ge lithiates, plastic strain accumulation can lead to an instability on the anode surface that forms V-shaped notches[8,10,12]. Theoretical modeling[13] has shown that this localization is a result of anisotropic motion of the c-Si/a-Li_xSi interface, which causes the crystalline core to develop sharp corners. These V-shaped notches can act as sites for crack nucleation[14]. However, this effect is particularly relevant for the first lithiation cycle only, as delithiation leaves silicon in an amorphous phase[15]. In a-Si or a-Ge, the motion of the phase transformation interface is isotropic, and the elastoplastic deformation retains the symmetry of the anode, e.g., a spherical distribution in the case of a spherical particle[15,16].

Lastly, researchers have experimented with anode shape as a means to improve stability. Experimental designs include thin films[17], nanoparticles[4], nanowires[7,10,18,19], nanopillars[20], hollow nanopillars[12], honeycomb[21], and many other novel configurations (see reviews[22,23]). Among these are promising designs using meso-, micro-, and nanoporous structures[24–29]. Using processes such as liquid metal dealloying (LMD)[24,25], vacuum distillation[26], and annealing and etching[27,28], it is possible to create smooth anode geometries with high surface area and thin ligaments. Such nanoporous structures have been shown to possess excellent stability, which is believed to be due to the structures' ability to accommodate the large volume expansion using pore space[24–26].

Beyond the high-level observations of pore space accommodation, there is limited insight into the mechanisms which underly the exceptional performance of nanoporous anodes. A notable experimental study was conducted by Zhao et al.[30]. Here, the authors used X-ray nano-tomography to image bulk nanoporous silicon anodes in lithium-ion batteries after various numbers of loading cycles. They

[1]Center for Interdisciplinary Research on Complex Systems, Department of Physics, Northeastern University, Boston, MA 02115, USA. [2]School of Engineering, Brown University, Providence, RI 02912, USA. ✉email: a.karma@northeastern.edu

found that there was heterogenous lithiation of the anodes, in particular at higher charge capacities, which led to a non-uniform expansion of the bulk anode and finally delamination from the current collector. The major damage mechanism of the anode was nanoporous particle agglomeration, which caused bulk mechanical damage and material loss, and disrupted lithium ion diffusion pathways. Computational studies into this problem are also rare, with ref. [29] being the only study of note. However, the computations in ref. [29] neglected several features of real nanoporous specimens. First, the specimen geometry was idealized with uniform thickness and periodic morphology. Second, the authors assumed spatially-uniform lithiation. In actuality, the phase transformation process is interface-limited, with an atomically sharp interface between lithiated and unlithiated phases[2]. Third, the authors decomposed the strain additively and assumed a linear elastoplastic constitutive response, which only applies for small strains rather than a 300% volume change.

In the present work, we seek to understand how spatially-heterogeneous shapes such as nanoporous structures behave when subjected to large swelling during lithium insertion and the factors that lead to their exceptional performance. In particular, we address the following questions. At a fundamental level, how does a nanoporous particle swell during lithiation, and how does it accommodate the large volume change? How do plastic strains and stresses develop and distribute throughout the structure? Compared with a model shape such as a sphere, how large are the stresses, how likely are the stresses to lead to fracture, and where might the fractures nucleate? Lastly, if the anodes were to break, how do fracture morphologies differ?

Within the discussion of stress and strain evolution, an important question relates to the formation of V-shaped notches as fracture nucleation sites. In this work, we do not explore anisotropic motion of the c-Si/a-Li_xSi interface, a driver of V-shaped notches in symmetric shapes, because anodes become amorphized after the first lithiation cycle. Nevertheless, in the case of a nanoporous shape, even for isotropic interface motion, the unlithiated core will initially be one connected domain like the starting structure, but it will generally become topologically disconnected as the lithiation front progresses further. Thus, the lithiation front may develop sharp corners (see Fig. 2 later in this work and the movies in the Supplementary Information), and we, therefore, address the question of whether these corners can potentially contribute to the localization of plastic deformation and fracture.

A nanoporous structure, such as those formed by dealloying, can be conceptualized as a network of ligaments connecting bulbous nodes. This raises the question of whether nodes or ligaments are mechanically more stable (conversely, more vulnerable to fracture) during swelling. The answer to this question is made highly non-trivial by the fact that the stiff unlithiated core becomes progressively more topologically disconnected as lithiation progresses, while the swelling lithiated medium remains a single domain. This makes swelling highly heterogeneous spatially, and hence its effect hard to predict.

To answer these questions, we perform a computational investigation of the lithiation-induced swelling behavior of nanoporous structures. The nanoporous specimens in our study were found through simulation of LMD[31,32]. Unlike ref. [29], we utilize a mechanical model which combines phase transformation with distinct unlithiated and lithiated phases, large deformation, elastoplasticity, and fracture. This model was previously used by the authors[14] to study lithiation and fracture of two-dimensional circles and annuli (representing infinite cylinders and tubes, respectively). Paired with the Finite Element Method, the mechanical model allows for the simulation of arbitrarily-shaped specimens. Other mechanical models and computational approaches exist in the literature (e.g. ref. [33]), and we refer the reader to ref. [34] for a review of the mechanical modeling of lithium-ion batteries.

Lastly, we summarize the model used herein. Further details about this model and its numerical implementation are recapitulated in the "Methods" section. Lithiation is modeled via a non-conserved order parameter ψ, whose value ranges from 0 (denoting unlithiated material) to 1 (fully-lithiated material). We assume that the lithium invasion occurs uniformly over the anode surface, which we believe is reasonable given that our simulations are for individual anode particles, rather than agglomerations of particles or entire anode structures. The interface between the two phases is diffuse, characterized by a small thickness w_ψ. The elastoplastic constitute response is neo-Hookean with J_2-plasticity and isotropic hardening[35–37]. The phase transformation induces isotropic strain β and a softening of the elastic moduli. Fracture is treated via the phase-field method, wherein a diffuse damage field ϕ (also taking a value between 0 and 1 for fully-broken and pristine material, respectively) with process zone size ξ evolves according to Ginzburg-Landau gradient dynamics[38]. In a large class of brittle materials, crack initiation is purely energetic; hence, the phase-field model is able to seamlessly incorporate both initiation and crack growth[39]. Driving crack evolution are tensile (i.e., non-compressive) and shear forces on the crack tip, here synthesized through the non-compressive strain energy density W^+. As a consequence of the phase-field model, damage onset occurs whenever W^+ exceeds a critical energy scale W_c (proportional to G_c/ξ).

RESULTS

Anode geometries

Here, we describe the reference configurations which were used in our computational study, see Fig. 1. Boundary conditions and material parameters may be found in the "Methods" section. The goal of this work is to understand how nanoporous morphology influences mechanical stability. For this study, we considered two nanoporous specimens, each of which was found through simulation of liquid metal dealloying and coarsening for parameters corresponding to TaTi alloys dealloyed by a pure Cu melt[31,40]. Liquid metal dealloying is controlled by the selective dissolution of one element of a solid binary alloy in the liquid melt, which produces a porous structure of the immiscible element. The porous structure coarsens during the dealloying process by diffusion of the immiscible element along the solid-liquid interface as well as by bulk liquid-state diffusion due the fact that the solubility of the immiscible element in the liquid is very small but finite[40]. Even though this alloy system differs from SiMg alloys dealloyed by a pure Bi melt, which was used to produce nanoporous Si in refs. [24,25], the Ta-rich and Si-rich dealloyed structures exhibit similar topologies.

The computed dealloyed structures in the TaTi/Cu system used in the present study are thus expected to be representative of the mechanical behavior of nanoporous Si when used in conjunction with mechanical properties of Si. In addition to differing alloy compositions (Ta25Ti75 and Ta30Ti70 in particles 1 and 2, respectively), the two structures corresponded to different levels of coarsening. Movies depicting the coarsening process for each are provided as Supplementary Information. The first particle was subjected to long-time coarsening, developing a well-defined ligament structure. Compared with a centroid-centered bounding sphere (cf. Fig. 1), the particle had 22.4% of the volume and 82.8% of the surface area. The second particle was taken early in the coarsening process; it had many holes, but not well-delineated ligaments. This particle had 34.4% of the volume and 143% of the surface area of its bounding sphere. Topologically, the first particle had genus 2, while the second had genus 30. Henceforth, we denote the particles as "low-genus" and "high-genus", respectively.

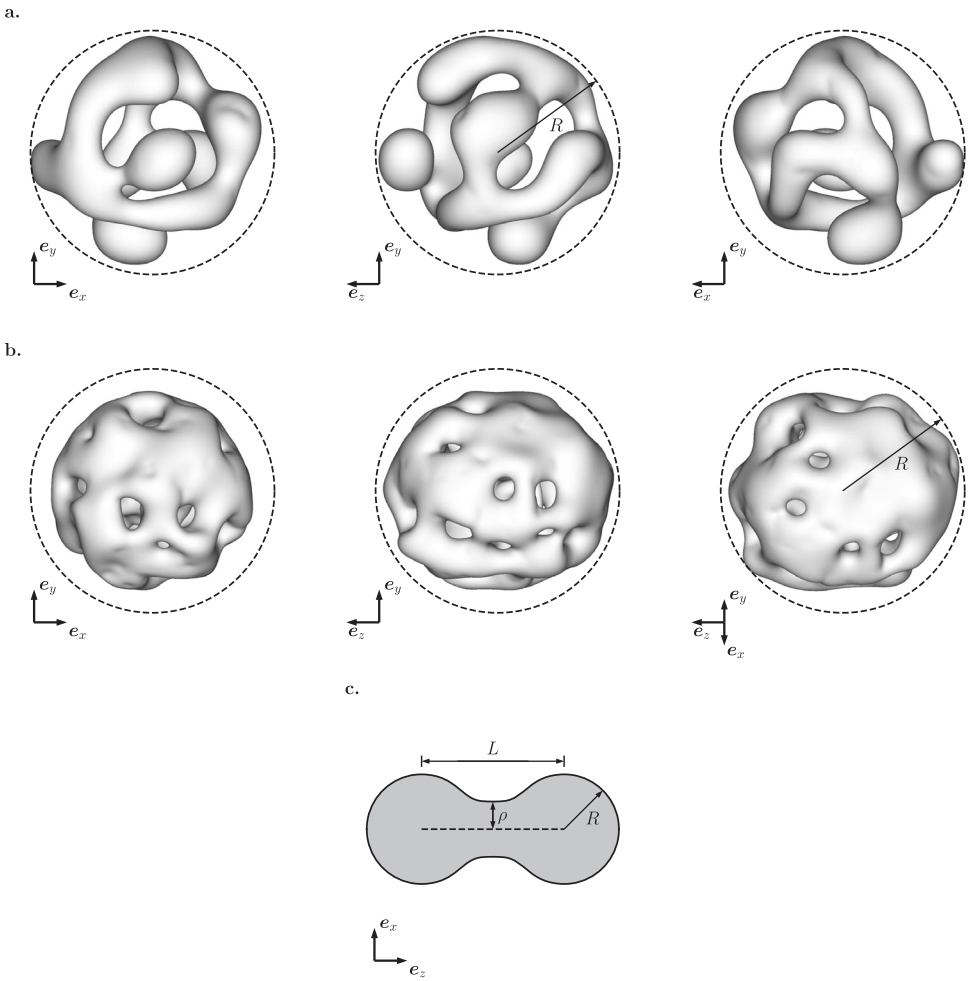

Fig. 1 Non-spherical anode geometries studied in this paper. a Low-genus particle and **b** high-genus particle, shown from three perspectives along with centroid-centered bounding sphere. **c** Barbell, shown from a top-down view. The spherical particle is not shown.

With greater coarsening, we believe that the low-genus particle better represented the nanoporous anodes of Wada et al.[24,25]. We idealized this structure as an interconnected network of ligaments and nodes. For comparison, we also considered the simplest ligament-node networks: a single sphere (i.e., a structure with no ligaments) and two spheres connected by a single ligament, which we call a "barbell". For the barbell geometries studied, the neck thickness was $\rho/R = 1/2$, while the neck length was either $L/R = 2.6$ ("short neck") or $L/R = 5.2$ ("long neck"). Both the sphere and barbells had genus 0. While not reported in this work, we also studied shapes with genus 1, such as the torus. We ultimately found that non-uniform thickness, already present in the barbell, was more important in understanding the swelling behavior of the nanoporous particles.

Shape change and the role of ligaments

We first address the question of how nanoporous anodes accommodate large volume change. We show snapshots of the deformation of the anodes in Fig. 2. Corresponding animations are provided in the Supplementary Information. Each snapshot is labeled with the percentage of the undeformed anode Ω_0 which has been lithiated, defined as:

$$\text{Percent lithiation} = \frac{100}{|\Omega_0|}\int_{\Omega_0} \psi \, dV. \quad (1)$$

We emphasize that computing the percent lithiation requires integrating the phase field ψ over the undeformed anode. As discussed in the "Methods" section, the phase transformation problem is cast with respect to the undeformed anode, and so this integration is straightforward in our simulations. The unlithiated core of the sphere remained spherical during the lithiation process. Because of the non-uniform specimen thickness, the unlithiated cores of the nanoporous particles and barbells became topologically disconnected. With its greater connectivity, more of the high-genus particle was lithiated before the core segmented.

As seen in Fig. 2, the low-genus particle experienced anisotropic structural expansion, notably preferring to elongate in the *y*-direction. To quantify this effect, we looked at the change in dimensions of the axis-aligned bounding box (AABB) for each shape, which we summarize in Table 1. The AABB was determined by shrinking a box, whose edges were parallel to the coordinate axes until each face was tangent to the contained volume. With the selected phase-transformation strain $\beta = 0.44$ (see the "Methods" section) and without rotation, isotropic expansion would cause the all three dimensions of the AABB to stretch by a factor of 1.44, which occurred for the sphere. In contrast, the *y*-dimension of the AABB of the low-genus particle stretched by 1.466 (measured as the length of dimension after lithiation divided by that before lithiation), while the stretch ratios of the *x*- and *z*-dimensions were ~1.28. Each dimension of the AABB of the high-genus particle was stretched by a factor around 1.36.

For the barbells, while the endcaps deformed like spheres, expansion in the axial direction (in the *z*-direction, along the ligament) was inhibited, with stretch factors 1.266 and 1.171 for

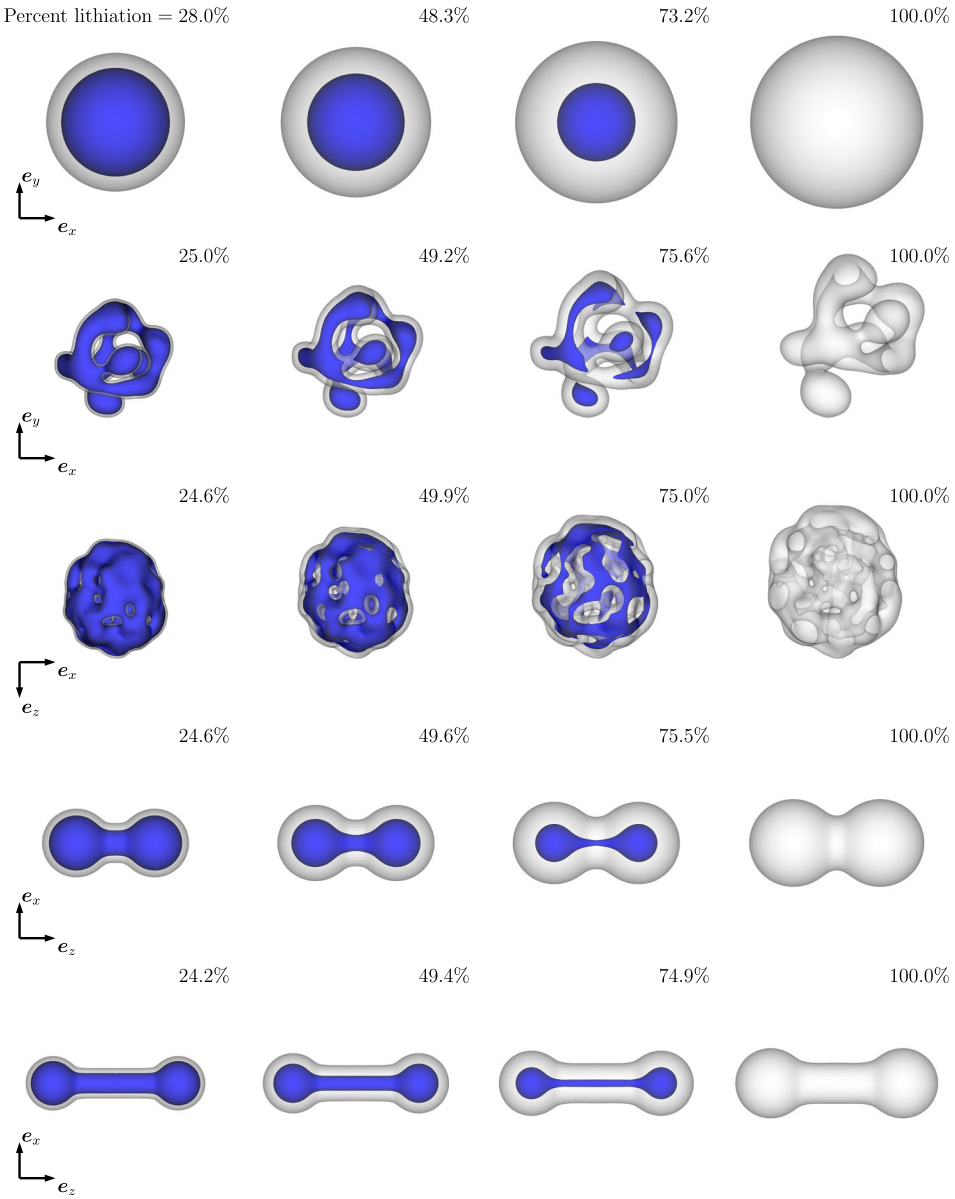

Fig. 2 (Top to bottom) Snapshots showing the lithiation of a sphere, low-genus particle, high-genus particle, short neck barbell, and long neck barbell. Each snapshot is labeled with the percent of the particle which has been lithiated, defined in (1). The blue surface shows the $\psi = 1/2$ isosurface, which is the boundary between unlithiated and lithiated material. During the lithiation process, the unlithiated core became topologically disconnected in the nanoporous particles and barbells (not shown).

the short neck and long neck specimens, respectively. Interestingly, the absolute changes in the axial (z) dimension were nearly identical, with values $1.224R$ and $1.234R$, respectively. For cylindrical shapes like the barbell with $L \gg R$, the amount of material lithiated from each end was controlled by the neck radius (i.e., the smallest dimension) rather than the cylinder length. Because unlithiated material was stiffer than lithiated material, the axial elongation resulted predominantly from the ends. Even after the ligament fully lithiated, plastic deformation prevented the material from relaxing axially. Hence, the axial strain was a decreasing function of ligament length, see Table 1. To accommodate the overall volume change, the ligament thickness had to increase by a factor exceeding 1.44; for the short and long ligaments, at $z = 0$ the radial stretch ratio was 1.821 and 1.712, respectively. In the case of an infinitely long ligament, we expect this ratio to approach $1.728 = 1.44^{3/2} = (1 + \beta)^{3/2}$.

The x- and z-dimension stretches (~1.28) in the low-genus particle were consistent with the axial stretches of the barbells. This supports the view of nanoporous particles as a network of ligaments and nodes. The large y-direction stretch in the low-genus particle may be due to the complete lithiation of certain ligaments. Once fully lithiated, ligaments were more compliant, which may have allowed the structure to reorient itself. In contrast, the high-genus particle had greater interconnectivity, which kept the core intact for longer during the lithiation process, and prevented reorientation of the structure.

We lastly comment on the change in volume of the AABB for each shape. The AABBs of the non-spherical shapes experienced smaller volumetric expansion than the nominal value $2.986 = 1.44^3 = (1 + \beta)^3$; for the low- and high-genus particles, the values were 2.417 and 2.522, respectively, while the short neck and long neck barbells had values 2.696 and 2.498, respectively. Hence, despite there being no external constraint on the particles,

Table 1. Dimensions of the axis-aligned bounding box (AABB) for the anode shapes in original and deformed configurations.

	Original [R]			Deformed [R]			Stretch ratio			Volume ratio
	x	y	z	x	y	z	x	y	z	
Sphere	2	2	2	2.881	2.881	2.879	1.441	1.441	1.440	2.987
Low-genus particle	1.880	1.859	1.910	2.411	2.726	2.455	1.282	1.466	1.285	2.417
High-genus particle	1.645	1.621	1.882	2.236	2.213	2.558	1.359	1.365	1.359	2.522
Short neck barbell	2	2	4.6	2.918	2.918	5.825	1.459	1.459	1.266	2.696
Long neck barbell	2	2	7.2	2.921	2.920	8.434	1.461	1.460	1.171	2.498

Also shown are the stretch ratio in each coordinate direction and the volume ratio of the AABBs.

with respect to the AABB the porosity decreased during lithiation. This result agrees with the perspective of Wada et al. (ref. [24], Fig. 1) that nanoporous structures accommodated volume change through decreased porosity. In our unconstrained structures, we reiterate that the porosity decreased because the ligaments resisted elongation, thereby necessitating the ligaments to grow thicker in orders to accommodate the overall volume change.

Plasticity, stress, damage, and fracture nucleation

For anisotropic interface mobility present in c-Si, sharp corners in the c-Si/a-Li_xSi interface promote the formation of V-shaped notches on the surface of spherical or cylindrical anodes[13], and these notches are potential nucleation sites for fracture[14]. We questioned if the same were true of the sharp corners that developed in the unlithiated cores of the nanoporous particles as they became topologically disconnected (for example, see the low-genus particle at 75% lithiation in Fig. 2). In Fig. 3, we show a non-dimensional measure of total plastic strain accumulation (which also quantifies isotropic hardening in the J_2-plasticity model, see the "Methods" section) on the anode surfaces at 100% lithiation. In spatially-heterogeneous shapes, sharp corners formed in ligaments after segmentation of the unlithiated core (see Fig. 2 and the corresponding movies in the Supplementary Information). For the barbells, the plastic strain accumulated preferentially at the connections between ligaments and spheres. In the nanoporous particles, the bulbous parts experienced larger plastic strains. In all specimens, no V-shaped notches formed, which suggested that corners resulting from segmentation of the unlithiated core did not cause plastic strain concentrations on the anode surfaces.

We next turn to the question of stress distribution in the nanoporous anodes. While we modeled phase transformation as isotropic volumetric expansion, geometric features like ligaments prevented axial elongation. In order to resist axial elongation, the unlithiated core of the ligament underwent tension. In Fig. 4, for two stages of lithiation, we show the regions of the spherical and low-genus anodes with the highest maximum tensile Cauchy stress, σ_1, along with the corresponding principal stress direction. These regions were computed by selecting the 5% of elements in the finite element mesh with the largest values of σ_1. Figures showing the regions for the other anode geometries may be found in the Supplementary Information. For the nanoporous particles, we removed a portion of the domain around the Dirichlet boundary to avoid polluting the data. Specifically, if the origin of our coordinate system is at the center of the bounding spheres (see Fig. 1), then we removed regions in the reference configuration with $y/R < -0.85$ for the low-genus particle and $z/R > 0.85$ for the high-genus particle. At all stages of lithiation, the maximum stresses in the sphere were those tangent to the surface. For the other shapes, during lithiation, there were large tensile stresses along the ligaments. At 100% lithiation, the maximum stresses in these shapes were also tangent to the surface.

In ref. [7], it was hypothesized that tensile stresses in the unlithiated core activated internal flaws which led to the destruction of nanowires. In contrast, analytical[9] and experimental[4] studies of spheres, and experimental studies of nanopillar arrays[8,12,20] suggested that flaws instead nucleated from the specimen surface. Damage originating from the surface seems to be further supported by observations of surface pulverization of nanoporous specimens (see ref. [24], Fig. S9 and ref. [5], Fig. S13).

Large tensile stresses alone are insufficient for predicting damage onset, as shearing stresses are neglected. For specimens with ligaments, the largest Cauchy stresses occurred within the unlithiated cores, whose material is demonstrably stiffer, though approximately as tough (cf. ref. [41], wherein the authors measured little dependence of the fracture toughness on lithium concentration in amorphous silicon, and ref. [42], wherein the fracture toughness of crystalline silicon is approximately the same value). We instead assessed damage onset and potential fracture nucleation sites using the energetic conditions from phase-field models of fracture[38,43] (see also the "Methods" section for the governing equations). In these models, damage nucleates whenever the non-compressive elastic energy W^+ (which synthesizes tension and shear) reaches a critical value W_c. The critical value W_c is proportional to G_c/ξ, where G_c is the fracture toughness of the material in the sharp-crack limit and ξ is the length scale of the phase-field process zone. In phase-field models, the length scale ξ sets the minimum crack size[39]. Here, the process zone has comparable length to the crack, and so that the damage field no longer sees the finite-length crack. When ξ is interpreted in this second way, the energetic criterion is equivalent to the Griffith approach to crack nucleation in traditional fracture mechanics. For nucleating a flaw with size ξ, the Griffith approach requires an energy balance between dissipated strain energy around the flaw (proportional to $W_c\xi^3$) and the energy of the newly created fracture surfaces (proportional to $G_c\xi^2$). Combined, these give $W_c \propto G_c/\xi$.

In Fig. 5, we plot the regions in each anode containing the highest values of W^+. Similar to those in Fig. 4, these regions represent the 5% of elements in the finite element mesh with the highest values of W^+. Again, we removed portions of the nanoporous particles around their Dirichlet boundaries. For all specimens, these regions were on the anode surface, which agreed with the previously discussed results. In particular, the highest W^+ values arose in the bulbous or spherical parts of the specimens.

We further analyzed the distribution of W^+ on the anode surfaces by plotting area histograms in the left column of Fig. 6. To compare different shapes, we normalized all surface areas by that of a sphere containing the same volume. As expected with rotational symmetry, the histogram for the sphere was concentrated around a single peak, whereas the nanoporous particles and barbells had broader distributions. Between 75 and 100% lithiation, the energy density decreased on large portions of the non-spherical anode surfaces, as evidenced by the broadening of

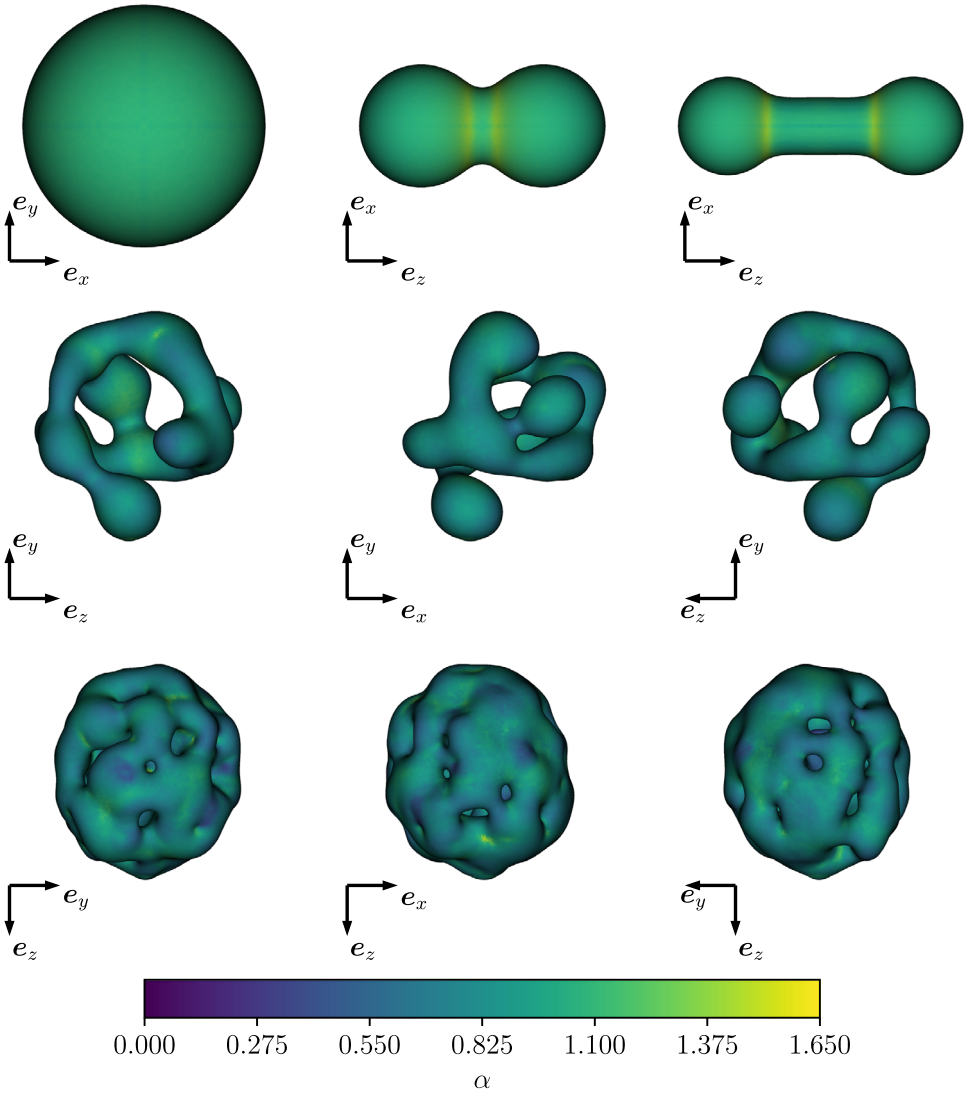

Fig. 3 Isotropic hardening parameter α, a measure of accumulated plastic strain, for the anodes studied at complete lithiation. (Top row) Sphere, short neck barbell, and long neck barbell. (Middle row) Low-genus particle, shown from three perspectives. (Bottom row) High-genus particle, shown from three perspectives. All anodes are shown in the deformed configuration. The distribution of α was symmetric on the surface of the sphere and on the spherical ends of the barbells. Plastic strain concentration did occur at the joints between sphere and neck in the barbells. For the nanoporous anodes, the bulbous regions experienced the largest plastic strains, with particular concentration on inner surfaces. No V-shaped notches formed in any of the specimens.

the lower energy tail of the histograms. This relaxation of the energy density coincided with the lithiation of the ligaments. While the maximum value of W^+ for the high-genus particle was nearly twice that of the sphere, such values were confined to very small regions on the surface. In contrast, for the other shapes, the maximum values of W^+ were comparable with that of the sphere. This indicated that the anode shape did not significantly impact the maximum value of W^+. Based on previous results[9,14], the stresses in the anodes were limited by the low yield stress, which in turn affected strains and strain energy density.

Because W^+ was comparable across all specimens, all specimens should damage during lithiation for a given value of W_c. However, surface damage does not necessarily lead to large-scale fracture and complete anode rupture, as sufficient driving force is needed to extend small surface cracks through the thickness. Here, the size effect resurfaces as a potential protective mechanism for the nanoporous particles, which will be demonstrated later. As discussed in the introduction, flaws in smaller particles are less likely to activate compared with those in larger particles for two reasons. First, larger particles are likely to have larger flaws, and from a dimensional analysis standpoint large flaws in large particles have a higher energy release rate G compared to small flaws in small particles. Second, flaws in smaller particles are more protected due to the gradient in the stress field. Because the anode surface is under tension while the core is under compression (cf. Fig. 7), the effective stress on a crack tip is reduced, as shown in ref. [4].

We further highlight the gradient effect by investigating where the anodes are under triaxial compression; in Fig. 7, we show the $\sigma_1 = 0$ isosurface at 100% lithiation. The compressive regions in the bulbous parts of the barbells and the low-genus particle occupied a similar proportion to that in the sphere; however, the bulbous parts were smaller, meaning the stress gradient was larger. Interestingly, the compressive regions were topologically disconnected at the joints of bulbous parts and ligaments. Comparing Figs. 7 and 5, in the barbells, these locations also had high W^+ values on the surface and were potential sites for fracture, whereas this was not the case for the low-genus particle.

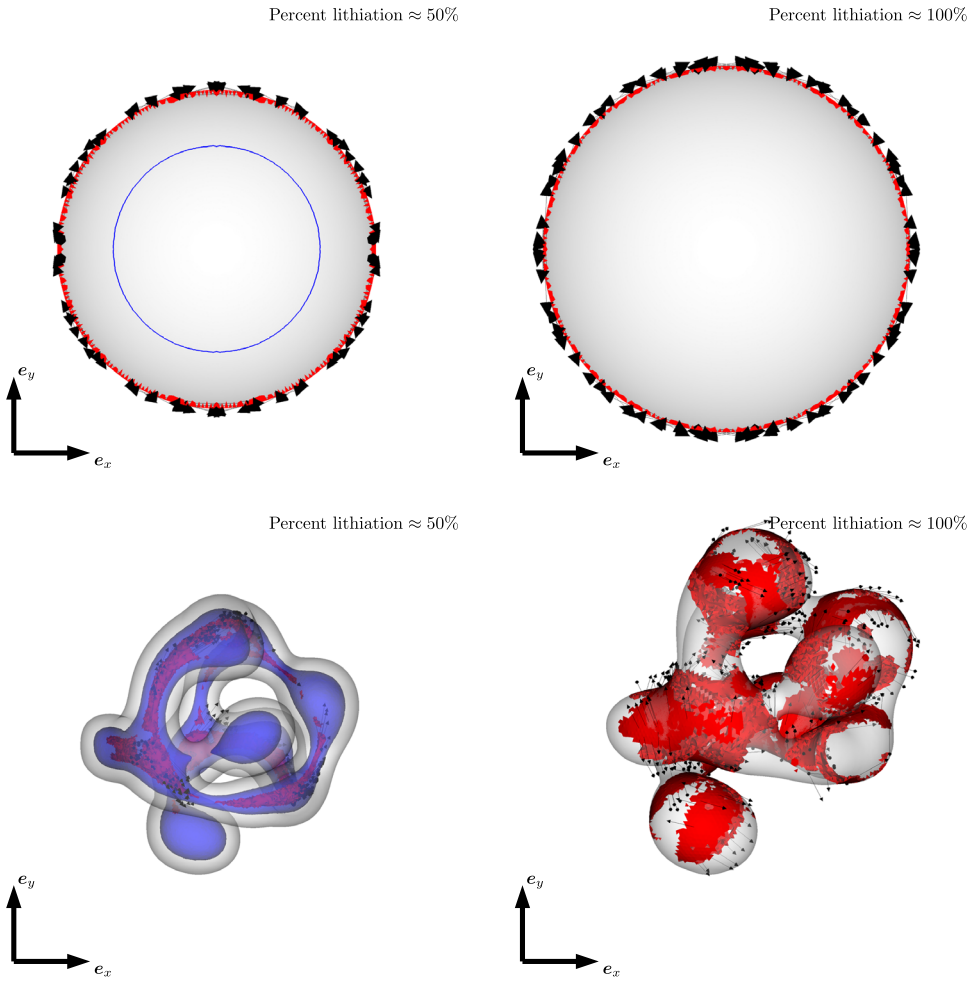

Fig. 4 Maximum tensile stress σ_1 at different stages of lithiation. The red volume shows the 5% of elements in the finite element mesh with the largest values of σ_1, while black arrows are the corresponding stress directions. The blue surface indicates the $\psi = 1/2$ isosurface, which marks the boundary between lithiated and unlithiated material. For the sphere, for ease of visibility we instead depict a slice through the middle of the specimen; here, the $\psi = 1/2$ boundary is shown as a blue contour. Anodes are shown in the deformed configuration.

A priori, it is unclear whether cracks would form only in regions with tensile stress (i.e., the gaps in the compressive region). We will revisit this question in the following subsection.

In addition to whether particles fracture, we also considered the extent to which fractures would nucleate. In the right column of Fig. 6, we plot the total surface area which has W^+ greater than a specified value, i.e., the cumulative distribution function of the histogram. These curves show how much surface area will damage for a given value of W_c. While the low-genus particle and high-genus particles had higher overall surface area than the sphere, less of the surface was vulnerable to damage. This result may have possible implications for the stability of the solid electrolyte interphase (SEI). Damage on the anode surface can destabilize the SEI, causing delamination[34] and even fragmentation[6], which results in further passivation of active material and capacity fade in Li-ion batteries. An interesting prospect for future work would be to explore how anode surface damage correlates with damage to the SEI.

Fracture

We lastly address the question of fracture morphology in nanoporous anodes by comparing the responses of the sphere and the low-genus particle. In this work, we did not consider concurrent lithiation and fracture as in ref. [14]; instead, we allowed the structure to lithiate fully, and then begin to break. Our rationale for this choice was due to two factors. First, in adapting the model and algorithms of ref. [14] to three-dimensional anodes, we found simulations with concurrent lithiation and fracture to be prohibitively slow and susceptible to convergence issues. These issues may have arisen from either the model or the solution algorithms. Referring to the Methods section, a potential area for improvement is the plasticity model. Currently, the model has no intrinsic length scale, which may cause issues in the combined presence of fracture and phase transformation, where large strain gradients may form. Other plasticity models (such as those with gradient terms[44] or based on alternate formulations like shear transition zones[45]) may alleviate these issues. From an algorithms standpoint, modifications to the traditional alternate minimization for phase-field fracture may be needed to more robustly solve the coupled equations (e.g. ref. [46]). Overall, the coupled problem of large deformation elastoplasticity, phase transformation, and fracture is highly non-linear. We believe that resolving these challenges to build a robust numerical method is fruitful area for further research.

Second, given the challenges in simulating concurrent lithiation and fracture, we observed that the largest stresses in the sphere occurred at 100% lithiation. This was generally not the case for the non-spherical shapes (as the structure relaxed when ligaments lithiated). Nevertheless, the reduction in energy density

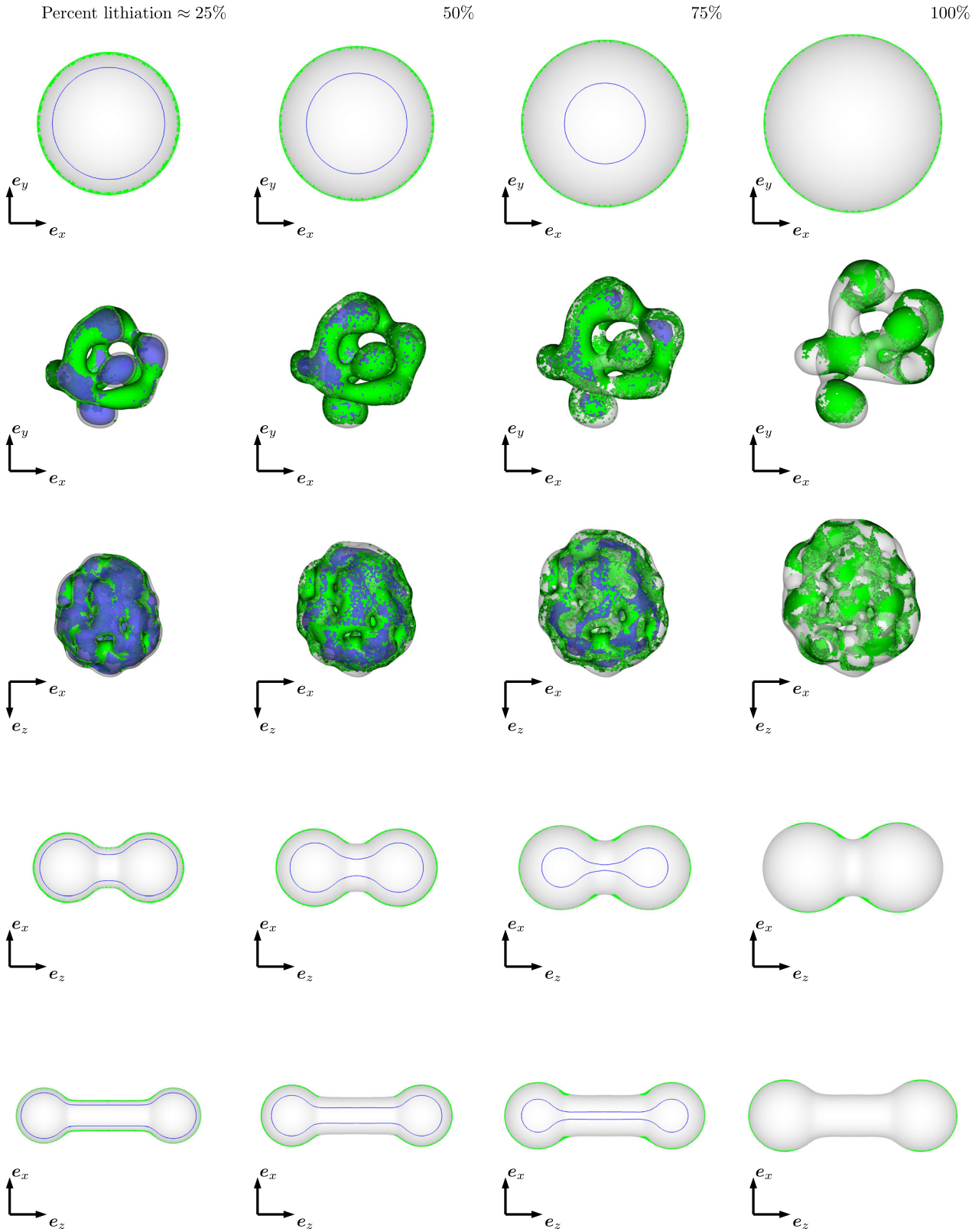

Fig. 5 Non-compressive elastic energy density W^+ at different stages of lithiation. The green volume shows the 5% of elements in the finite element mesh with the largest values of W^+. The blue surface indicates the $\psi = 1/2$ isosurface, which marks the boundary between lithiated and unlithiated material. For the sphere and barbells, for ease of visibility we instead depict a slice through the middle of the specimen; here, the $\psi = 1/2$ boundary is shown as a blue contour. Anodes are shown in the deformed configuration.

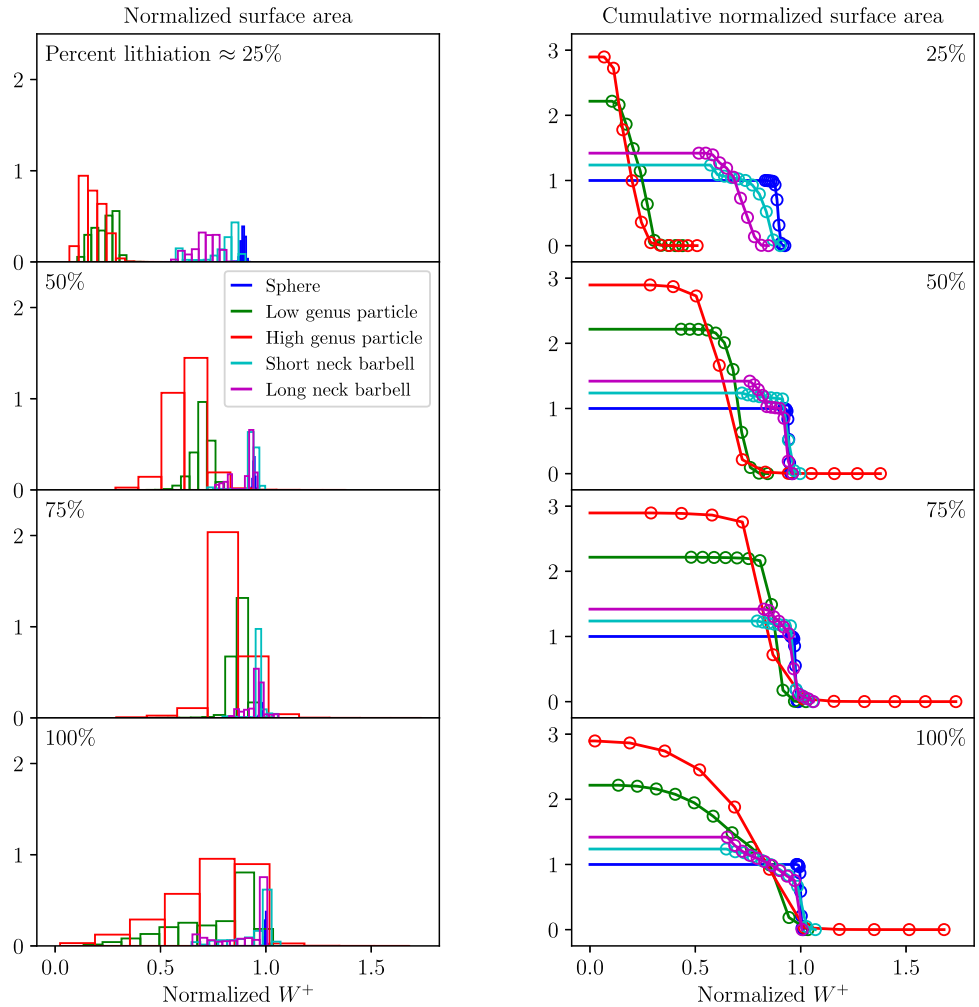

Fig. 6 (Left) Histograms depicting the variation in W^+ on the surface of the anodes. The bar heights represent the total surface area with W^+ between the left and right sides of the bar. (Right) Cumulative distribution functions of W^+ on the anode surface. The height of each point is the total surface area with W^+ at or exceeding the abscissa value. The values of W^+ have been normalized by the mean value for the sphere at 100% lithiation. For each anode, the surface area has been normalized by that of a sphere enclosing the same reference volume. Surface areas are computed with respect to the reference configuration.

experienced on some portions of the anode surface did not substantially reduce the largest magnitudes of the driving stresses of fracture (see Fig. 6). Additionally, there are uncertainties associated with the locations of preexisting flaws in manufactured specimens. Hence, we expect that our choice of initial condition would not strongly affect our conclusions regarding the relative mechanical stability of the spherical and nanoporous particles.

With the exception of the width w_ψ, which defines the interface thickness in the phase transformation process, the stress fields in the anodes are size-independent. Anode size only is important when selecting fracture toughness G_c and phase-field process zone size ξ for crack nucleation. From experimental data[41], the fracture toughness is around 6 J m^{-2}. Meanwhile, experiments show the fracture process zone size to be very small[4,41], on the order of 10 nm or less[33]. Referring to the Methods section, this gives a value of $W_c = 0.225$ GJ m^{-3}.

To ensure our specimens fractured for the observed values of W^+ in Fig. 6, we set $W_c = 0.0225$ GJ m^{-3}, which is smaller than the previous value by a factor of 10. We chose $\xi/R = 0.05$ so that fractures were small compared with the overall specimen size. Hence, our fracture simulations may be viewed either as occurring in a large sample with $R = 2$ µm and $G_c = 6$ J m^{-2}, or a smaller sample having smaller G_c (e.g., $R = 200$ nm and $G_c = 0.6$ J m^{-2}).

We show the damage field evolution in Fig. 8. For the sphere, ϕ degraded uniformly on the surface before breaking the spherical symmetry and localizing into a network of cracks. The resulting crack pattern included fragmentation on the surface, while some cracks grew deep into the specimen. We remark that the eight-fold symmetry of the fracture patterns was a consequence of that of the simulation. However, the formation of a network of surface cracks is reminiscent of fracture patterns in intercalation electrodes[47].

Compared with the sphere, the low-genus particle saw damage onset at each bulbous part, but not along the ligaments. These damage zones quickly coalesced into fractures; one for each spherical region. The cracks did not completely rupture the specimen, and no fragmentation was observed. Instead, the cracks stopped about halfway through each bulb. As mentioned previously, the smaller thickness of the bulbs and ligaments acted to protect the low-genus particle from complete rupture. In contrast with the rotationally symmetric spherical particle, the bulbous parts of the low-genus particle were non-uniform, which facilitated the coalescence of damage into cracks and prevented large amounts of damage to the specimen surface. Lastly, the fractures did not appear to interact, with each crack growing independently of the others. One possible interpretation is that the plastic strains in the ligaments acted as a buffer, preventing

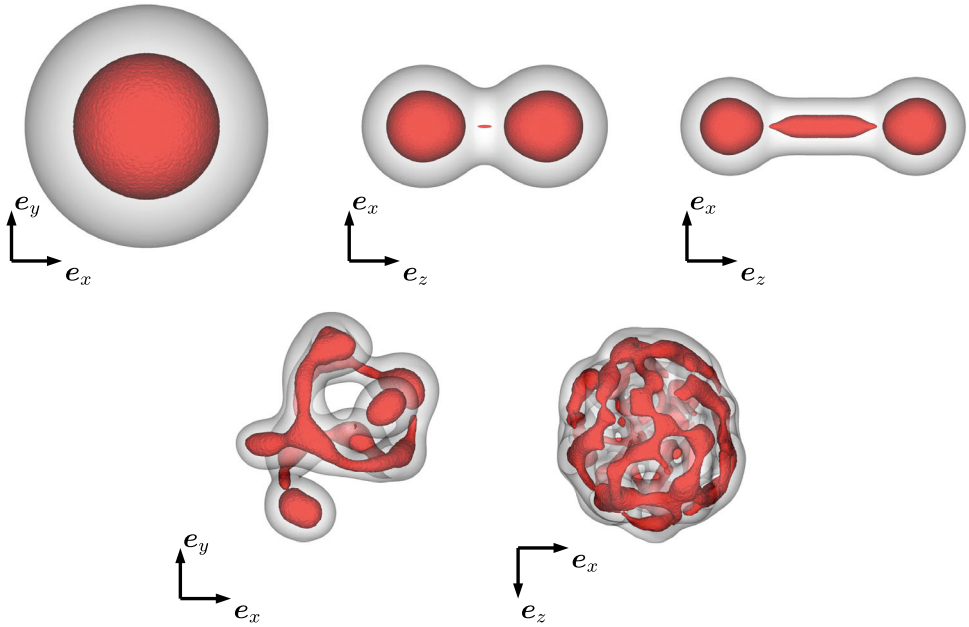

Fig. 7 Isosurface of maximum principle stress $\sigma_1 = 0$ for the anodes studied at complete lithiation. Within the red isosurface, the material is under triaxial compression. Anodes are depicted in the deformed configuration.

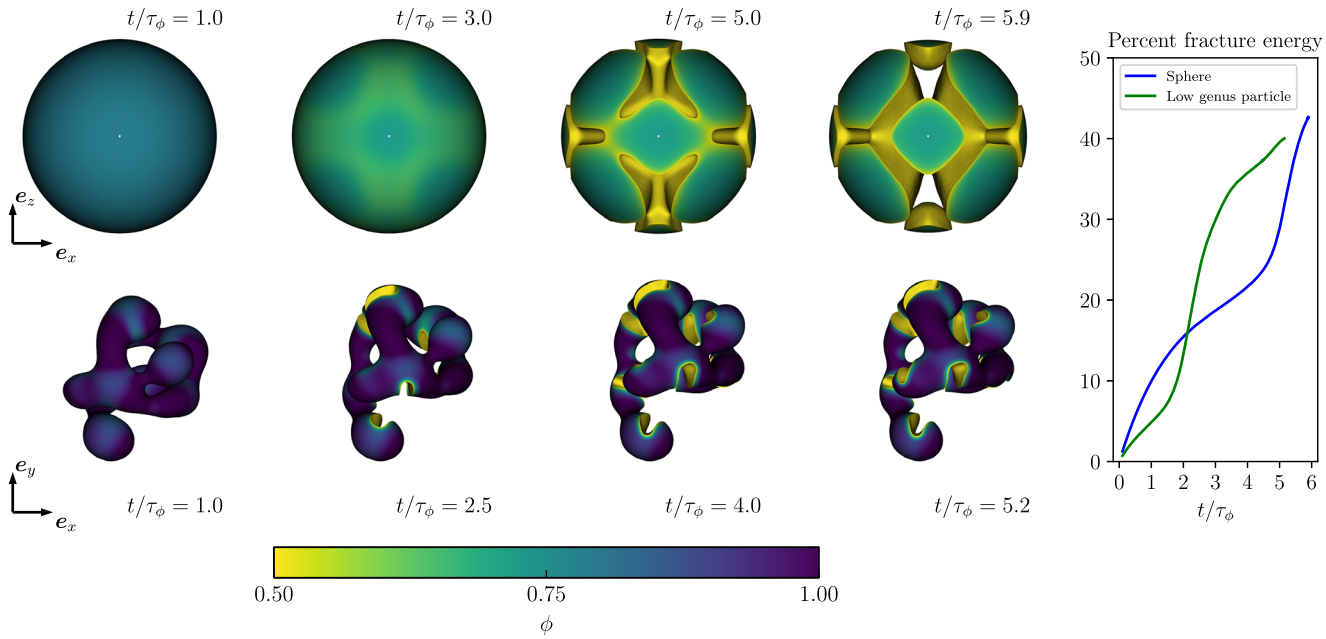

Fig. 8 (Left) Crack evolution for the sphere and low-genus particle. Particles are shown in the deformed configuration, and regions with $\phi < 1/2$ have been removed. The sphere damaged uniformly before cracks localized, and the cracks led to fragmentation of the surface. The low-genus particle fractured in numerous places, corresponding with the bulbous parts and the connections between ligaments. These fractures did not completely rupture particle. (Right) Percentage of fracture energy versus relaxation time, $100\frac{\mathcal{F}_\phi(t)}{\mathcal{F}_e(0)}$. Fracture energies have been normalized by the strain energy of the anode at full lithiation.

stress relaxation from being transmitted between nodes/bulbous parts. In this way, crack growth in one node would not relax the stresses around a crack in a second node. This result further supports the view of the low-genus particle as a collection of spheres connected by ligaments.

We lastly plotted the phase-field fracture energy for the sphere and low-genus particle in Fig. 8 as a percentage of that particle's strain energy at full lithiation (i.e., $100\frac{\mathcal{F}_\phi(t)}{\mathcal{F}_e(0)}$). In the limit as ξ is reduced, the phase-field fracture energy will approach G_c times the sharp crack surface area. We note two behaviors. First, both anodes experienced rapid fracture growth, although this occurred later for the sphere. As mentioned previously, the bulbs of the low-genus particle were non-uniform, which expedited the coalescence of damage into cracks. Second, the percentages of fracture energy are similar between the two specimens; however, per unit volume, the sphere had a greater strain energy at full lithiation (~0.0164 J mm^{-3}) compared to the low-genus particle (~0.0129 J mm^{-3}). Hence, for a given anode volume, the

low-genus particle had less overall fracture energy (i.e., less surface area) compared with the sphere.

We conclude by returning to the question of fracture before 100% lithiation. We conducted simulations where the low-genus and spherical particles were at 50 and 75% lithiation using the above parameters. Here, we fixed the lithiation field ψ and allowed the fracture phase field to evolve. We believe this modeling assumption is well-motivated by the large discrepancy between experimentally measured lithiation front speeds[15] and the shear wave speed in amorphous silicon (cf. the "Methods" section for further discussion). At both lithiation percentages and for both particles, we did not observe the formation of damage or fractures. This suggests that for both particles, damage would initiate after 75% lithiation. Because the stress states in both particles were similar at 75 and 100% lithiation, we do not expect significant differences in the fracture behavior that what was observed above.

DISCUSSION

In this work, we utilized a multi-physics mechanical model—incorporating phase transformation, elastoplastic deformation, and fracture—to reveal insights into the swelling behavior of nanoporous structures during lithium insertion that underly their exceptional performance as anodes in lithium-ion batteries (e.g. refs. [24,25]). For this task, we simulated nanoporous specimens with realistic shapes created through simulation of liquid metal dealloying[31,32], and we compared these shapes with idealized geometries.

At a fundamental level, we found that ligaments in the nanoporous structures resisted elongation, which led to overall anisotropic expansion of the low-genus particle and loss of porosity of both low- and high-genus particles with respect to their bounding volumes. Even without external constraint, the nanoporous specimens expanded into the pores via thickening of the ligaments. This effect would be more pronounced for constrained specimens, for example the graphene-coated nanoporous particles in ref. [27]. Meanwhile, the bulbous parts and the connections between ligaments and nodes were preferential sites for plastic strain accumulation. However, despite the sharp corners in the lithiation front which formed after the unlithiated core became topologically disconnected, plastic strain concentrations and V-shaped notches were not observed on the specimen surfaces. With regards to stress distribution, the ligaments also experienced the largest tensile stresses within the unlithiated cores in order to resist axial elongation.

Because the unlithiated core was much stiffer than the surrounding lithiated material, tensile stresses alone were insufficient to predict fracture onset. Instead, we turned to an energetic criterion observed in a large class of brittle materials and well simulated using phase-field models. Here, an energy density synthesizing both tensile and shear stresses drove fracture. We remark that the energetic criterion, with critical energy W_c, is equivalent to the standard Griffith approach in fracture mechanics for initiation of flaws with size ξ. In the Griffith approach to fracture, energy balance implies that the strain energy dissipated around a flaw (proportional to $W_c\xi^3$) equals the energy of the created fracture surface (proportional to $G_c\xi^2$); consequently, $W_c \propto G_c/\xi$. In phase-field models, the energy criterion drives the onset of diffuse damage, which may be interpreted as the activation of preexisting flaws or the formation of new flaws in the material at the characteristic length scale ξ. Under the energetic criterion, we predicted damage and fracture to occur on the specimen surfaces, notably around the bulbous parts and not the ligaments, which aligned with previous theory[9] and experimental observations[4,8,12,20].

Interestingly, the maximum values of the driving energy W^+ were comparable across specimens, due to the low yield threshold limiting the stress magnitudes[14]. This implied that for a given material with critical energy W_c (equivalently, toughness G_c and critical flaw size ξ) all anode geometries would either damage or not. Hence, the dominant protective mechanism in the nanoporous anodes was the size effect (combining dimensionality considerations and stress gradient effects). As revealed by our simulations, the low-genus particle behaved like a network of spheres connected by ligaments, each with smaller thickness than a uniform sphere with the same overall volume. Simulations of fracture growth after lithiation further demonstrated the protective nature for the low-genus particle, where cracks in the bulbous regions failed to rupture the specimen. Experiments show[4] that fractures may develop before complete lithiation; hence, to fully understand how the size effect protects the nanoporous structures, it is necessary in the future to run computations featuring concurrent phase transformation and fracture evolution. However, as discussed in the fracture section, there are a number of challenges which need to be overcome, ranging from the inclusion of intrinsic length scale in the plasticity model to specialized numerical solution procedures for the elasticity, plasticity, and damage fields. Further computational mechanics research is needed to devise stable and robust algorithms to simulate the highly non-linear concurrent problem.

Although the nanoporous particles had high surface area compared with a sphere of identical volume, less overall surface area would damage at a given value of W_c. This result may relate to the stability of the solid-electrolyte interphase (SEI), as less damage on the anode surface may correspond to less damage to the SEI. However, to better quantify the effect, lithiation models which include SEI growth and mechanical deformation are needed. The SEI is generally heterogenous and composed of various chemical species[48], and its composition depends on the electrolyte and operating conditions[49].

There are also questions of how the mechanical behavior and stability of individual nanoporous particles affect those of a bulk lithion-ion battery anode, as in the experiments of Zhao et al.[30]. Along with the interaction with the SEI described previously, it is unclear how the deformation and damage of individual nanoporous particles (and agglomeration with neighboring particles) would contribute to damage in the bulk, compared to an equivalent bulk anode composed of spherical particles.

In this work, we used fairly simple models for the elastoplastic and fracture behaviors of the anode material. The choice to use J_2-plasticity was motivated by its ability to reproduce stress measurements in thin films[50] as well as qualitatively the shapes of deformed nanowires (e.g. refs. [10,13]). More elaborate models could be used, for example the plasticity models in refs. [51,52] which incorporate stress relaxation effects observed in atomistic studies[53]). For the fracture model, given the small scales of nanoporous silicon structures, one could also incorporate surface tension effects (cf. [54,55]).

Lastly, this work highlighted how geometric features of the nanoporous particles affected their mechanical behavior. Advanced anode designs also make use of material composites. For example, in ref. [27], the authors encased nanoporous silicon particles in a silicon and graphene shell. Meanwhile, in ref. [5], the authors fabricated a sandwich design of graphene, silicon, and hybrid silicate in the form of a shell of a nanoporous structure. The use of multiple materials in composite anode particles greatly expands the design space. It also raises questions of how these materials interact and impact the stability of the particle. Because the mechanical model in this work can be extended to include multiple materials, it may be used to better understand the swelling behavior of composite designs, an exciting prospect for future work.

METHODS

Model

We use the mechanical model of[14] to describe the evolution of the anode during lithiation. We recapitulate the details here. We model the lithiation and subsequent deformation of an anode with finite-strain J_2 elastoplasticity[35–37]. We assume that the deformation occurs quasi-statically (i.e., neglecting inertial effects); for anode materials like a-Si, the speed of lithium invasion is several orders of magnitude slower than elastic wave speeds[15]. The lithiation process is described via Ginzburg-Landau phase-transition kinetics of a non-conserved order parameter ψ. The parameter ψ takes a value between 0 and 1; respectively, these indicate the unlithiated and fully-lithiated material, see Fig. 9. Lithiation is assumed to start uniformly on the anode surface. The effect of lithiation on the elastoplastic response is two-fold. First, lithiation induces a linear expansion of the material due to the reorganization of the atomic structure. Second, the lithiated material is more compliant. We ignore the effect of mechanical stress on the reaction rate (cf. [34]).

After lithiation, we consider fracture of the specimen. Here, the fracture is described via the evolution of a continuous phase-field ϕ. When $\phi = 1$, the material is pristine, while fully damaged material has $\phi = 0$. The particular phase-field model is AT1 (see ref. [43] for fundamental details, and[56] for application to non-linear elastoplasticity), which allows for both crack nucleation and propagation.

We briefly comment on vector and tensor notation used in the remainder of this paper, which are differentiated from scalar quantities via bold symbols. We let (x, y, z) denote the Cartesian coordinates of the vector $\mathbf{x} = x\mathbf{e}_x + y\mathbf{e}_y + z\mathbf{e}_z$.

Kinematics of the anode. Due to the large volume change, we must distinguish between the reference (equivalently, undeformed, initial, or unlithiated) configuration, Ω_0, and the deformed (partially-lithiated) configuration Ω_t at time t (see Fig. 9). Points in Ω_t are expressed through the deformation (or the displacement) mapping $\mathbf{x}_t = \boldsymbol{\varphi}(t, \mathbf{x}_0) = \mathbf{x}_0 + \mathbf{u}(t, \mathbf{x}_0)$. We use the same subscripts to differentiate operators with respect to reference and deformed coordinates; for example, if $f : \Omega_0 \to \mathbb{R}$, then $\mathrm{grad}_0 f = \partial f / \partial \mathbf{x}_0 : \Omega_0 \to \mathbb{R}^3$.

We assume a multiplicative decomposition[50,57] of the deformation gradient $\mathbf{F} := \mathrm{grad}_0 \boldsymbol{\varphi} = \mathbf{F}_\mathrm{e}\mathbf{F}_\mathrm{p}\mathbf{F}_\psi$. In this way, the deformation is the combination of expansion due to phase transformation, plastic deformation, and elastic deformation. The expansion is assumed to be volumetric with form $\mathbf{F}_\psi = (1 + \beta\psi)\mathbf{1}$, where β denotes the linear expansion coefficient. Plastic deformation is assumed to be isochoric, $J_\mathrm{p} = \det(\mathbf{F}_\mathrm{p}) = 1$; hence $J = \det(\mathbf{F}) = \det(\mathbf{F}_\mathrm{e})\det(\mathbf{F}_\psi) = J_\mathrm{e}J_\psi = J_\mathrm{e}(1 + \beta\psi)^3$.

The kinematic variables in our formulation are the displacement field $\mathbf{u}$ (or the deformation $\boldsymbol{\varphi}$) and the order parameter ψ. We next describe how these variables evolve. Included in our formulation will be internal variables that describe the plastic deformation.

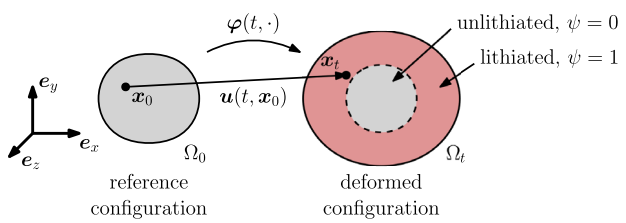

Fig. 9 Reference and deformed geometry of the anode. In our model, the state of lithiation is described by an order parameter ψ, which varies smoothly from unlithiated ($\psi = 0$) to fully-lithiated ($\psi = 1$) values.

Elastoplasticity. We write the elastic energy in terms of the strain energy density:

$$\mathcal{F}_\mathrm{e}[\mathbf{u}, \psi] = \int_{\Omega_0} W(\mathbf{F}_\mathrm{e}, \psi)\, \mathrm{d}V_0. \tag{2}$$

We assume the elastic constitutive response is neo-Hookean. Following ref. [37], we use:

$$W(\mathbf{F}_\mathrm{e}, \psi) = \frac{\mu(\psi)}{2}\left(\mathrm{tr}(\hat{\mathbf{b}}_\mathrm{e}) - 3\right) + \frac{\kappa(\psi)}{4}\left(J_\mathrm{e}^2 - 2\log J_\mathrm{e} - 1\right) \tag{3}$$

where $\hat{\mathbf{b}}_\mathrm{e} = J_\mathrm{e}^{-2/3}\mathbf{F}_\mathrm{e}\mathbf{F}_\mathrm{e}^T$ is the isochoric elastic left Cauchy-Green deformation tensor and $\mathrm{tr}(\cdot)$ denotes the trace operator. We model the effect of lithiation on the elastic properties through the law of mixtures for shear and bulk moduli (μ and κ, respectively):

$$\mu(\psi) = \mu_\mathrm{l}\psi + \mu_\mathrm{u}(1 - \psi) \text{ and } \kappa(\psi) = \kappa_\mathrm{l}\psi + \kappa_\mathrm{u}(1 - \psi), \tag{4}$$

where subscripts u and l denote the unlithiated and fully-lithiated states, respectively.

As in ref. [37], we write the yield condition with isotropic hardening in terms of the Kirchhoff stress tensor $\boldsymbol{\tau}$:

$$\sqrt{\mathrm{dev}(\boldsymbol{\tau}) : \mathrm{dev}(\boldsymbol{\tau})} \le \sqrt{\frac{2}{3}}(\sigma_\mathrm{Y} + K\alpha) \tag{5}$$

where $\mathrm{dev}(\boldsymbol{\tau}) = \boldsymbol{\tau} - \frac{1}{3}\mathrm{tr}(\boldsymbol{\tau})\mathbf{1}$ is the deviatoric part of $\boldsymbol{\tau}$, σ_Y is the yield threshold, α is a hardening parameter, and K is the isotropic hardening modulus. From our strain energy density function, the Kirchhoff stress is computed:

$$\boldsymbol{\tau} = \mu(\psi)\mathrm{dev}(\hat{\mathbf{b}}_\mathrm{e}) + \frac{\kappa(\psi)}{2}\left(J_\mathrm{e}^2 - 1\right)\mathbf{1}.$$

We remark that the state of plasticity is given by the path-dependent variables $\hat{\mathbf{b}}_\mathrm{e}$ and α, which measure the amount of elastic strain (and hence plastic strain) and the isotropic hardening, respectively.

Finally, for a given ψ, the displacement field solves:

$$\left.\frac{\delta \mathcal{F}_\mathrm{e}}{\delta \mathbf{u}}\right|_{\psi, \mathbf{F}_\mathrm{p}, \alpha \text{ fixed}} = \mathrm{div}_t(\boldsymbol{\sigma}) = \mathbf{0}, \tag{6}$$

together with the constraint Eq. (5), where $\delta\mathcal{F}_\mathrm{e}/\delta\mathbf{u}$ is the Fréchet derivative of the free energy with respect to the displacement field and $\boldsymbol{\sigma} = J^{-1}\boldsymbol{\tau}$ is the Cauchy (true) stress tensor.

Phase transformation. The Ginzburg-Landau free energy for the order parameter is written:

$$\mathcal{F}_\psi[\psi] = h_\psi \int_{\Omega_0} \left(F(\psi) + w_\psi^2 |\mathrm{grad}_0\, \psi|^2\right) \mathrm{d}V_0, \tag{7}$$

where h_ψ is the energy barrier height between unlithiated and lithiated states and w_ψ characterizes the thickness of the phase transformation interface. We take $F(\cdot)$ as a combination of double-well and forcing potentials:

$$F(\psi) = 4\psi^2(1 - \psi)^2 + \Delta g(\psi) \tag{8}$$

with the function:

$$g(\psi) = 1 - 10\psi^3 + 15\psi^4 - 6\psi^5 \tag{9}$$

that varies monotonically between 0 in the lithiated phase ($g(1) = 0$) and 1 in the unlithiated phase ($g(0) = 1$) and has vanishing first and second derivatives at $\psi = 0$ and 1. With this choice, the bulk free-energy of the unlithiated phase is raised by an amount $\Delta > 0$ above the bulk free-energy of the lithiated phase, thereby driving the lithiated phase to invade the unlithiated phase.

The order parameter then evolves according to:

$$\tau_\psi \frac{\partial \psi}{\partial t} = -\frac{1}{h_\psi}\frac{\delta \mathcal{F}_\psi}{\delta \psi} = -\left[F'(\psi) - 2w_\psi^2 \mathrm{div}_0(\mathrm{grad}_0\, \psi)\right]. \tag{10}$$

where τ_ψ is a time constant. The prior equation assumes isotropic mobility of the reaction front. In crystalline silicon, the mobility has been shown to exhibit anisotropy[8,10,13]. Anisotropy may be incorporated through a suitable prefactor of the right-hand side[13,14]; this is not considered in this work.

We now discuss the role of the time constant τ_ψ. In diffuse interface models, the resulting interface velocity scales with the ratio w_ψ/τ_ψ and has contributions from interface curvature and from the forcing potential intensity Δ. In previous work[14], mobility anisotropy was the dominant effect; hence, a small Δ was sufficient to drive the reaction. For the isotropic mobility of lithiation of a-Si, experiments show that the interface speed is nearly constant[15]. Because the shapes studied have multiple curvatures and thicknesses, we seek to minimize curvature effects by selecting a large Δ.

Ultimately, in the coupled elastoplasticity and phase transformation problem, time only appears through the evolution of the order parameter ψ. As mentioned, the time constant controls the diffuse interface speed. This means that if we wanted to reproduce a desired interface speed v, we should set $\tau_\psi \propto \Delta w_\psi/v$, where we have assumed that the curvature effects are small.

Fracture. When considering situations with crack nucleation and growth, the mechanical energy consists of the sum of elastic and fracture parts: $\mathcal{F}_e$ and $\mathcal{F}_\phi$. The fracture energy is:

$$\mathcal{F}_\phi[\phi] = \frac{3G_c}{8\xi}\int_{\Omega_0}\left((1-\phi)+\xi^2|\mathrm{grad}_0\,\phi|^2\right)\mathrm{d}V_0 \tag{11}$$

where G_c is the fracture toughness of the material in the sharp-crack limit and ξ is the length scale characterizing the thickness of the phase-field. The prefactor $\frac{3G_c}{8\xi}$ (henceforth termed W_c) defines a critical energy for fracture nucleation[43]. Following[14,56], we decompose the strain energy density into isochoric and volumetric parts:

$$W^+(\mathbf{F}_e,\psi) = \frac{\mu(\psi)}{2}(\mathrm{tr}(\hat{\mathbf{b}}_e)-3) + \begin{cases} \frac{\kappa(\psi)}{4}\left(J_e^2 - 2\log J_e - 1\right) & J_e \geq 1, \\ 0 & J_e<1, \end{cases} \tag{12}$$

$$W^-(\mathbf{F}_e,\psi) = \begin{cases} 0 & J_e \geq 1, \\ \frac{\kappa(\psi)}{4}\left(J_e^2 - 2\log J_e - 1\right) & J_e<1, \end{cases} \tag{13}$$

and we impose that only tensile volumetric parts contribute to fracture growth. Hence, the total elastic energy $\mathcal{F}_e$ is modified:

$$\mathcal{F}_e[\mathbf{u},\phi,\psi] = \int_{\Omega_0}\left((\phi^2+\eta_\epsilon)W^+(\mathbf{F}_e,\psi)+W^-(\mathbf{F}_e,\psi)\right)\mathrm{d}V_0, \tag{14}$$

where η_ϵ is a small parameter to prevent the equations from becoming singular in fully-broken material.

We evolve the phase-field according to the Ginzburg-Landau equation[38]:

$$\tau_\phi\frac{\partial\phi}{\partial t} = -\frac{1}{W_c}\frac{\delta(\mathcal{F}_e+\mathcal{F}_\phi)}{\delta\phi} = -\left[2\phi\frac{W^+(\mathbf{F}_e,\psi)}{W_c} - 1 - 2\xi^2\mathrm{div}_0(\mathrm{grad}_0\,\phi)\right] \tag{15}$$

for some time constant τ_ϕ. Additionally, we must impose irreversibility of the damage process:

$$\frac{\partial\phi}{\partial t} \leq 0 \tag{16}$$

along with the bounds $0 \leq \phi \leq 1$.

In our fracture model, only the elastic deformation drives damage evolution. Plastic deformation dissipates energy from the system. This model is sometimes referred to as "brittle fracture in elastoplastic solids"[58]. In the context of phase-field models for fracture, other models exist which couple damage and plastic evolution[58]. These models are based on notions of void nucleation and coalescence ahead of the crack tip and are particularly developed for ductile fracture of metals where the shear band formation facilitates the crack propagation. However, this phenomenon has not been experimentally observed in lithiation of nanoscale anode particles, and hence for simplicity we do not include its effect in the above fracture model.

For coupled phase transformation and fracture, the relative scaling of the respective time constants τ_ψ and τ_ϕ is important. From experiments of fracture in lithiating anodes[4], we have that $\tau_\phi < \tau_\psi$. This relationship between τ_ϕ and τ_ψ can also be inferred from estimates of the lithiation interface speed and elastic wave speed in amorphous silicon[15]. If we estimate the speed of lithiation from the thickness of the lithiated layer of an amorphous silicon sphere (ref. [15], Fig. 3), the value is on the order of nm s^{-1}. Meanwhile, from the material parameters of silicon (see the "Model parameters" section below for elastic moduli and ref. [59] for density), the shear wave speed is on the order of km s^{-1}. However, in this work, we do not consider concurrent phase transformation and fracture, and hence we do not explicitly specify either time scaling. Rather, time t/τ may be viewed as a parameterization of the evolution of the corresponding field (ψ or ϕ).

Numerical method

Our numerical procedure is similar to that of Mesgarnejad and Karma[14], and we refer the reader there for an outline. Here, we highlight differences in our approach, and we summarize the boundary conditions and model parameters used in our study.

Approximation spaces. We partition the domain Ω_0 into a mesh $\mathcal{T}_h$ of non-overlapping tetrahedral elements with maximum diameter h. The tetrahedra in our meshes are approximately uniform in size. On this mesh, we define the finite element function space $P^1(\Omega_0)$ (resp. $P^2(\Omega_0)$), whose members are continuous and linear (resp. quadratic) on each element $E \in \mathcal{T}_h$. We approximate the displacement field in $P^2(\Omega_0;\mathbb{R}^3)$ in order to alleviate locking phenomena that can occur during fully plastic flow (cf. [60,61]). Meanwhile, the order parameter ψ and the fracture phase-field ϕ are approximated in $P^1(\Omega_0)$. Plasticity variables $\hat{\mathbf{b}}_e$ and α are stored at the quadrature points.

Elastoplastic update. Given ψ, we solve the elastoplastic problem using the radial return algorithm of ref. [37], which enables both the update of the displacement field and the plastic variables. We modify the radial return algorithm following ref. [56] to ensure that $\det(\hat{\mathbf{b}}_e) = 1$. As shown in ref. [56], preserving the condition $\det(\hat{\mathbf{b}}_e) = 1$ is important for predicting the correct evolution of the elastic energy during plastic flow.

Initializing the simulations. We desire our simulations to begin with $\psi = 1$ on the boundary of the domain. This situation corresponds to uniform lithium invasion across the entire surface of the particle. Starting simulations with this condition imposed presents two problems. The large volume change means that the correct deformed state is sufficiently far from the reference configuration, which precludes solving the elastoplasticity equations. Hence, we increment ψ from 0 to 1 on the boundary. However, with the forcing potential, ψ will propagate inward, even before reaching 1 on the boundary. Our solution to this problem is to begin the simulations by imposing a negative forcing amplitude (here, flipping the sign of Δ) and slowly (i.e., over the interval $[0, 10\tau_\psi]$) raising ψ from 0 to 1 on the external boundaries. The negative forcing amplitude prevents the phase transition from propagating into the domain, thereby yielding a thin boundary layer of phase-transformed material. From this state, we apply a positive forcing amplitude, and we let the simulations proceed.

Boundary conditions. For shapes with octahedral symmetry, we simulated only a single octant. Mirror boundary conditions were

imposed on the three symmetry planes. The choice of such boundary conditions precluded the possible appearance of symmetry-breaking modes during non-linear elastoplastic deformation and during fracture. Further study is required to see if asymmetric modes exist. Referring to Fig. 1, setting the origin of our coordinate system to be the center of the bounding spheres, for the low-genus particle, we held fixed the patch of boundary triangles with $y_0/R < -0.91$ (all of which belonged to a single bulbous protrusion). To ensure the choice of grip did not impact results away from the Dirichlet boundary, we also considered a specimen with $z_0/R > 0.96$ fixed and found the results to be nearly identical. Meanwhile, for the high-genus particle, we held fixed those triangles with $z_0/R > 0.91$.

Model parameters. We used the same material parameters as in ref. [14], which were comparable to experimentally measured values of silicon and germanium (e.g. refs. [13,62]). The unlithiated and lithiated elastic moduli were $(\kappa_u, \mu_u) = (108\,\text{GPa}, 50\,\text{GPa})$ and $(\kappa_l, \mu_l) = (10.8\,\text{GPa}, 5\text{GPa})$, respectively. The plasticity parameters were $\sigma_Y = 0.5\,\text{GPa}$ and $K = 0.05\,\text{GPa}$. It was shown in ref. [14] that the isotropic hardening modulus K had little impact on the final results. To ensure 300% volume expansion during lithiation, we set $\beta = 0.44$. For the phase transformation, we took the driving force $\Delta = 15/16$ to minimize interface curvature effects, while the diffusion width w_ψ was set equal to the mesh size of our simulations. In all specimens, the mesh size h was selected as $R/h = 40$.

DATA AVAILABILITY

The data sets generated during the current study are available from the corresponding author on reasonable request.

CODE AVAILABILITY

The code and workflow developed in this study are available from the authors upon reasonable request.

Received: 8 July 2022; Accepted: 12 May 2023;
Published online: 29 June 2023

REFERENCES

1. Park, C.-M., Kim, J.-H., Kim, H. & Sohn, H.-J. Li-alloy based anode materials for Li secondary batteries. *Chem. Soc. Rev.* **39**, 3115–3141 (2010).
2. Liu, X. H. et al. In situ atomic-scale imaging of electrochemical lithiation in silicon. *Nat. Nanotechnol.* **7**, 749–756 (2012).
3. Beaulieu, L. Y., Eberman, K. W., Turner, R. L., Krause, L. J. & Dahn, J. R. Colossal reversible volume changes in lithium alloys. *Electrochem. Solid State Lett.* **4**, A137 (2001).
4. Liu, X. H. et al. Size-dependent fracture of silicon nanoparticles during lithiation. *ACS Nano* **6**, 1522–1531 (2012).
5. Huang, G. et al. Ultrastable silicon anode by three-dimensional nanoarchitecture design. *ACS Nano* **14**, 4374–4382 (2020).
6. Wu, H. et al. Stable cycling of double-walled silicon nanotube battery anodes through solid–electrolyte interphase control. *Nat. Nanotechnol.* **7**, 310–315 (2012).
7. Ryu, I., Choi, J. W., Cui, Y. & Nix, W. D. Size-dependent fracture of Si nanowire battery anodes. *J. Mech. Phys. Solids* **59**, 1717–1730 (2011).
8. Lee, S. W., McDowell, M. T., Berla, L. A., Nix, W. D. & Cui, Y. Fracture of crystalline silicon nanopillars during electrochemical lithium insertion. *Proc. Natl Acad. Sci. USA* **109**, 4080–4085 (2012).
9. Zhao, K. et al. Concurrent reaction and plasticity during initial lithiation of crystalline silicon in lithium-ion batteries. *J. Electrochem. Soc.* **159**, A238–A243 (2012).
10. Liu, X. H. et al. Anisotropic swelling and fracture of silicon nanowires during lithiation. *Nano Lett.* **11**, 3312–3318 (2011).
11. Lee, S. W., Ryu, I., Nix, W. D. & Cui, Y. Fracture of crystalline germanium during electrochemical lithium insertion. *Extrem. Mech. Lett.* **2**, 15–19 (2015).
12. Zhang, X.-Y. et al. Geometric design of micron-sized crystalline silicon anodes through in situ observation of deformation and fracture behaviors. *J. Mater. Chem. A* **5**, 12793–12802 (2017).
13. An, Y. et al. Mitigating mechanical failure of crystalline silicon electrodes for lithium batteries by morphological design. *Phys. Chem. Chem. Phys.* **17**, 17718–17728 (2015).
14. Mesgarnejad, A. & Karma, A. Vulnerable window of yield strength for swelling-driven fracture of phase-transforming battery materials. *npj Comput. Mater.* **6**, 1–10 (2020).
15. McDowell, M. T. et al. In situ TEM of two-phase lithiation of amorphous silicon nanospheres. *Nano Lett.* **13**, 758–764 (2013).
16. Berla, L. A., Lee, S. W., Ryu, I., Cui, Y. & Nix, W. D. Robustness of amorphous silicon during the initial lithiation/delithiation cycle. *J. Power Sources* **258**, 253–259 (2014).
17. Graetz, J., Ahn, C. C., Yazami, R. & Fultz, B. Highly reversible lithium storage in nanostructured silicon. *Electrochem. Solid State Lett.* **6**, A194 (2003).
18. Chan, C. K. et al. High-performance lithium battery anodes using silicon nanowires. *Nat. Nanotechnol.* **3**, 31–35 (2008).
19. Liu, X. H. et al. Ultrafast electrochemical lithiation of individual Si nanowire anodes. *Nano Lett.* **11**, 2251–2258 (2011).
20. Ye, J. et al. Enhanced lithiation and fracture behavior of silicon mesoscale pillars via atomic layer coatings and geometry design. *J. Power Sources* **248**, 447–456 (2014).
21. Baggetto, L., Danilov, D. & Notten, P. H. L. Honeycomb-structured silicon: remarkable morphological changes induced by electrochemical (de)lithiation. *Adv. Mater.* **23**, 1563–1566 (2011).
22. Sun, Y., Liu, N. & Cui, Y. Promises and challenges of nanomaterials for lithium-based rechargeable batteries. *Nat. Energy* **1**, 1–12 (2016).
23. Wu, H. & Cui, Y. Designing nanostructured Si anodes for high energy lithium ion batteries. *Nano Today* **7**, 414–429 (2012).
24. Wada, T. et al. Bulk-nanoporous-silicon negative electrode with extremely high cyclability for lithium-ion batteries prepared using a top-down process. *Nano Lett.* **14**, 4505–4510 (2014).
25. Wada, T., Yamada, J. & Kato, H. Preparation of three-dimensional nanoporous Si using dealloying by metallic melt and application as a lithium-ion rechargeable battery negative electrode. *J. Power Sources* **306**, 8–16 (2016).
26. An, Y. et al. Green, scalable, and controllable fabrication of nanoporous silicon from commercial alloy precursors for high-energy lithium-ion batteries. *ACS Nano* **12**, 4993–5002 (2018).
27. Wang, J. et al. Surface-engineered mesoporous silicon microparticles as high-Coulombic-efficiency anodes for lithium-ion batteries. *Nano Energy* **61**, 404–410 (2019).
28. Wang, J. et al. Scalable synthesis of nanoporous silicon microparticles for highly cyclable lithium-ion batteries. *Nano Res.* **13**, 1558–1563 (2020).
29. Zuo, X. et al. Rational design and mechanical understanding of three-dimensional macro-/mesoporous silicon lithium-ion battery anodes with a tunable pore size and wall thickness. *ACS Appl. Mater. Interfaces* **12**, 43785–43797 (2020).
30. Zhao, C. et al. Imaging of 3D morphological evolution of nanoporous silicon anode in lithium ion battery by X-ray nano-tomography. *Nano Energy* **52**, 381–390 (2018).
31. Geslin, P.-A., McCue, I., Gaskey, B., Erlebacher, J. & Karma, A. Topology-generating interfacial pattern formation during liquid metal dealloying. *Nat. Commun.* **6**, 1–8 (2015).
32. Lai, L. *Phase-field Modeling of Crystalline Nanostructures Formed by Vapor-Liquid-Solid Growth and Liquid Metal Dealloying*. Ph.D. thesis, Northeastern University (2020).
33. Zhang, X., Krischok, A. & Linder, C. A variational framework to model diffusion induced large plastic deformation and phase field fracture during initial two-phase lithiation of silicon electrodes. *Comput. Methods Appl. Mech. Eng.* **312**, 51–77 (2016).
34. Zhao, Y. et al. A review on modeling of electro-chemo-mechanics in lithium-ion batteries. *J. Power Sources* **413**, 259–283 (2019).
35. Simo, J. A framework for finite strain elastoplasticity based on maximum plastic dissipation and the multiplicative decomposition: Part I. Continuum formulation. *Comp. Methods Appl. Mech. Eng.* **66**, 199–219 (1988).
36. Simo, J. A framework for finite strain elastoplasticity based on maximum plastic dissipation and the multiplicative decomposition. Part II: Computational aspects. *Comp. Methods Appl. Mech. Eng.* **68**, 1–31 (1988).
37. Simo, J. C. & Hughes, T. J. *Computational Inelasticity (Interdisciplinary Applied Mathematics, Vol. 7)* (Springer Science & Business Media, 1998).
38. Karma, A., Kessler, D. A. & Levine, H. Phase-field model of mode III dynamic fracture. *Phys. Rev. Lett.* **87**, 045501 (2001).
39. Tanné, E., Li, T., Bourdin, B., Marigo, J.-J. & Maurini, C. Crack nucleation in variational phase-field models of brittle fracture. *J. Mech. Phys. Solids* **110**, 80–99 (2018).
40. Lai, L., Gaskey, B., Chuang, A., Erlebacher, J. & Karma, A. Topological control of liquid-metal-dealloyed structures. *Nat. Commun.* **13**, 1–10 (2022).
41. Pharr, M., Suo, Z. & Vlassak, J. J. Measurements of the fracture energy of lithiated silicon electrodes of Li-ion batteries. *Nano Lett.* **13**, 5570–5577 (2013).

42. Chen, C. P. & Liepold, M. H. Fracture toughness of silicon. *Am. Ceram. Soc. Bull.* **59**, 469–472 (1980).
43. Bourdin, B., Francfort, G. A. & Marigo, J.-J. The variational approach to fracture. *J. Elast.* **91**, 5–148 (2008).
44. Cottura, M. et al. A phase field model incorporating strain gradient visco-plasticity: application to rafting in Ni-base superalloys. *J. Mech. Phys. Solids* **60**, 1243–1256 (2012).
45. Rycroft, C. H. & Bouchbinder, E. Fracture toughness of metallic glasses: annealing-induced embrittlement. *Phys. Rev. Lett.* **109**, 194301 (2012).
46. Brach, S., Tanné, E., Bourdin, B. & Bhattacharya, K. Phase-field study of crack nucleation and propagation in elastic-perfectly plastic bodies. *Comp. Methods Appl. Mech. Eng.* **353**, 44–65 (2019).
47. Mesgarnejad, A. & Karma, A. Phase field modeling of chemomechanical fracture of intercalation electrodes: role of charging rate and dimensionality. *J. Mech. Phys. Solids* **132**, 103696 (2019).
48. Nanda, J. et al. Unraveling the nanoscale heterogeneity of solid electrolyte interphase using tip-enhanced Raman spectroscopy. *Joule* **3**, 2001–2019 (2019).
49. Wang, A., Kadam, S., Li, H., Shi, S. & Qi, Y. Review on modeling of the anode solid electrolyte interphase (SEI) for lithium-ion batteries. *npj Comput. Mater.* **4**, 1–26 (2018).
50. Bower, A., Guduru, P. & Sethuraman, V. A finite strain model of stress, diffusion, plastic flow, and electrochemical reactions in a lithium-ion half-cell. *J. Mech. Phys. Solids* **59**, 804–828 (2011).
51. Levitas, V. I. & Attariani, H. Anisotropic compositional expansion and chemical potential for amorphous lithiated silicon under stress tensor. *Sci. Rep.* **3**, 1–5 (2013).
52. Levitas, V. I. & Attariani, H. Anisotropic compositional expansion in elasto-plastic materials and corresponding chemical potential: large-strain formulation and application to amorphous lithiated silicon. *J. Mech. Phys. Solids* **69**, 84–111 (2014).
53. Zhao, K. et al. Reactive flow in silicon electrodes assisted by the insertion of lithium. *Nano Lett.* **12**, 4397–4403 (2012).
54. Levitas, V. I., Jafarzadeh, H., Farrahi, G. H. & Javanbakht, M. Thermodynamically consistent and scale-dependent phase field approach for crack propagation allowing for surface stresses. *Int. J. Plast.* **111**, 1–35 (2018).
55. Jafarzadeh, H., Farrahi, G. H., Levitas, V. I. & Javanbakht, M. Phase field theory for fracture at large strains including surface stresses. *Int. J. Eng. Sci.* **178**, 103732 (2022).
56. Borden, M. J., Hughes, T. J., Landis, C. M., Anvari, A. & Lee, I. J. A phase-field formulation for fracture in ductile materials: finite deformation balance law derivation, plastic degradation, and stress triaxiality effects. *Comp. Methods Appl. Mech. Eng.* **312**, 130–166 (2016).
57. Lee, E. H. Elastic-plastic deformation at finite strains. *J. Appl. Mech.* **36**, 1–6 (1969).
58. Alessi, R., Ambati, M., Gerasimov, T., Vidoli, S. & De Lorenzis, L. Comparison of phase-field models of fracture coupled with plasticity. In *Advances in Computational Plasticity: A Book in Honour of D. Roger J. Owen*, (eds Oñate, E., Peric, D., de Souza Neto, E., & Chiumenti M.) 1–21 (Springer International Publishing, 2018).
59. Custer, J. S. et al. Density of amorphous Si. *Appl. Phys. Lett.* **64**, 437–439 (1994).
60. Hughes, T. J. *The Finite Element Method: Linear Static and Dynamic Finite Element Analysis* (Courier Corporation, 2000).
61. Wriggers, P. *Nonlinear Finite Element Methods* (Springer-Verlag, 2008).
62. Pharr, M., Choi, Y. S., Lee, D., Oh, K. H. & Vlassak, J. J. Measurements of stress and fracture in germanium electrodes of lithium-ion batteries during electrochemical lithiation and delithiation. *J. Power Sources* **304**, 164–169 (2016).

ACKNOWLEDGEMENTS

This work was supported by the U.S. Department of Energy, Office of Basic Energy Sciences through grant DE-FG02-07ER46400. Northeastern University's Discovery cluster, a part of the Massachusetts Green High Performance Computing Center (MGHPCC), was used for most of the simulations. Our simulations also took advantage of computational resources under the auspices of XSEDE allocation MSS200005. We thank Dr. Longhai Lai for providing the nanoporous geometries and the movies depicting coarsening.

AUTHOR CONTRIBUTIONS

B.E.G.P., A.M., and A.K. conceived the theoretical study, interpreted the numerical results, and wrote the paper. B.E.G.P. carried out the numerical study.

COMPETING INTERESTS

The authors declare no competing interests.

ADDITIONAL INFORMATION

Supplementary information The online version contains supplementary material available at https://doi.org/10.1038/s41524-023-01047-y.

Correspondence and requests for materials should be addressed to Alain Karma.

Reprints and permission information is available at http://www.nature.com/reprints

Publisher's note Springer Nature remains neutral with regard to jurisdictional claims in published maps and institutional affiliations.